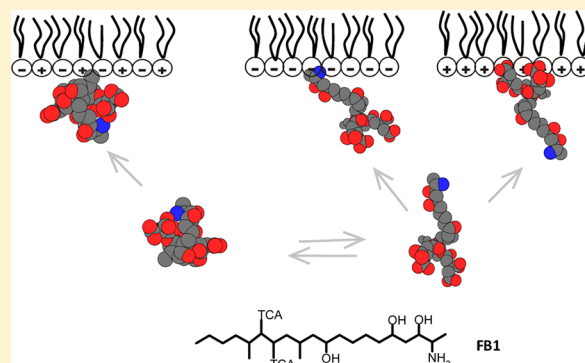


Effect of Surface Charge on the Interfacial Orientation and Conformation of FB1 in Model Membranes

Martín G. Theumer,^{†,‡} Pedro D. Clop,[†] Héctor R. Rubinstein,[‡] and María A. Perillo^{*,†}

[†]IIByT, CONICET - Química Biológica, Depto. Química, Facultad de Ciencias Exactas Físicas y Naturales and [‡]CIBICI, CONICET - Microbiología de los alimentos, Depto. Bioquímica Clínica, Facultad de Ciencias Químicas, Universidad Nacional de Córdoba, Ciudad Universitaria, Córdoba, Argentina

ABSTRACT: The toxicity of FB1 is usually explained through the enzymatic disruption of lipidic metabolism. However, it may lie in the thermodynamics of the membrane and its cooperative phase behavior rather than in the activity of individual proteins. Here, we investigate the effects of FB1 at the molecular and mesoscopic levels in FB1–phospholipid mixed Langmuir films. Mean molecular area vs FB1 molar fractions (x_{FB1}) and phase diagram analysis allowed us to define miscibility conditions and phase states at different x_{FB1} . Surface potential measurements, evaluated as a function of the molecular packing and x_{FB1} , revealed the FB1-induced change in the collective dipolar reorientation led to neutralization of charged films. Size, shape, and distribution of 2D-domain analysis from epifluorescence data suggested the increase in the mixing entropy and film relaxation rate. Finally, PM-IRRAS revealed the orientation of FB1 with the amine end (zwitterionic and negatively charged monolayers) pointing to the air. The globular-extended conformational equilibrium of FB1 is dynamically defined by the membrane charge becoming a toxicity enhancing factor. The specificity of the toxin–protein interaction might also be perturbed by the FB1-induced remodeling of the membrane topography by affecting the raft-like platforms where membrane enzymes are considered to be located.



1. INTRODUCTION

Mycotoxins are naturally occurring toxic compounds produced by a wide variety of molds frequently found as contaminants of agricultural commodities and byproducts worldwide. Most of these secondary metabolites are toxic for human beings, animals, and plants, which has led to their use as chemical weapons on several occasions since the Middle Ages.¹ Paradoxically, several non-naturally occurring derivatives of ergot, a toxin synthesized by the fungus *Claviceps purpurea*, are currently being used as therapeutic drugs for the treatment of diseases such as parkinsonism, hyperprolactinemia, and cerebrovascular insufficiency.²

Nowadays, health problems in populations chronically exposed to “low doses” of mycotoxins through the diet and the economical losses caused by these substances in the food industry are of major concern.

Fumonisin B1 (FB1) is a mycotoxin mainly produced by toxigenic stocks of *Fusarium verticillioides* (Sacc.) Nirenberg (e.g., *F. moniliforme* Sheldon) and *F. proliferatum* (Matsushima) Nirenberg, and belongs to a group of at least 28 fumonisins commonly classified as B- (the most important ones due to their toxicity and their occurrence in nature), A- (*n*-acetylated congeners), C- (which lack the terminal methyl), and P-series (structurally identical to the B series except that the members have a 3-hydroxypyridinium functional group in place of the C-2 amine group).³ The structure of FB1 consists of a 20-carbon backbone with an amine group at C2, three hydroxyl groups at

C3, C5, and C10, two methyl groups at C12 and C16, and two tricarballylic acid monoester groups at C14 and C15.

The toxicology of FB1 appears to be mainly related with the competitive inhibition of ceramide synthase (CS). This is expected to be associated with the structural similarities that the toxin bears with some CS substrates which are long-chain sphingoid bases such as sphinganine and sphingosine.⁴ Moreover, since the hydrolyzed derivative of FB1 (the aminopentol 1, AP1) is less effective in inhibiting the CS activity, it was proposed that both the amino group (sphingoid-binding domain) as well as the tricarballylic acid side chains (fatty acyl CoA domain) of FB1 are involved in such biological effect.⁵ However, Bionda and co-workers⁶ observed that FB1 increased the *in vitro* Sprague–Dawley rat mitochondrial CS activity when sphingosine was used as the substrate. In accordance with the hypothesis previously proposed by Venkataraman et al.,⁷ the authors suggested that more than one (dihydro)-CS and/or CS may coexist within the cell and in various subcellular organelles, based on evidence regarding either their fatty acid specificity or their difference in FB1 sensitivity.

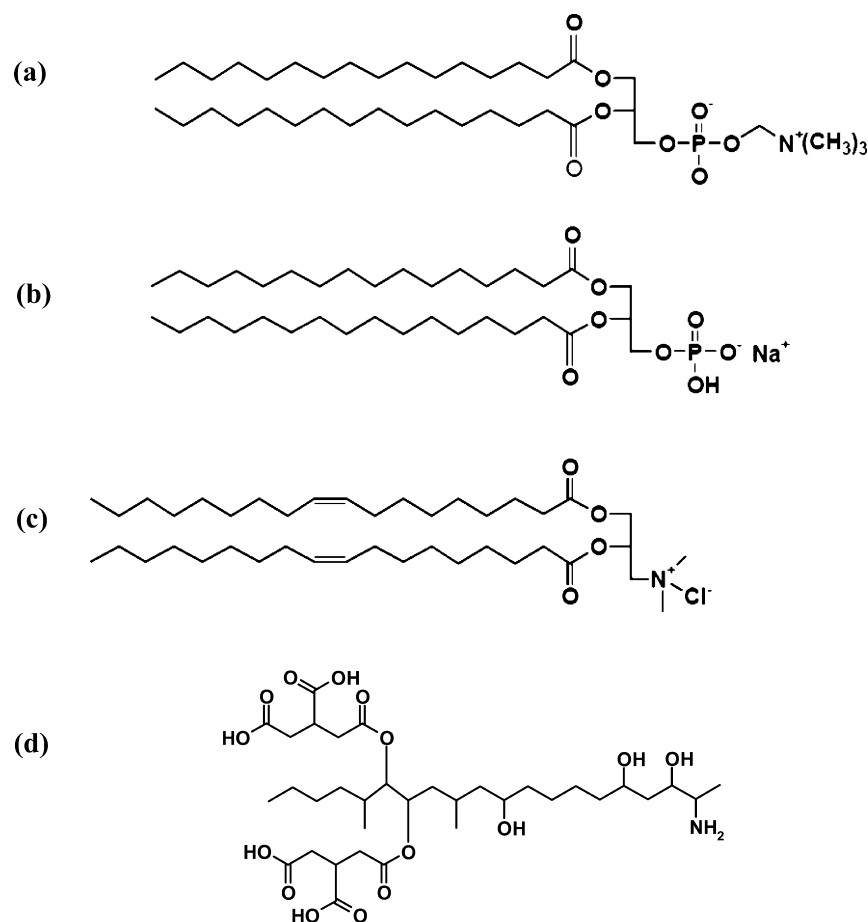
Apart from the modulating effect that FB1 might exert in the CS activity by its direct action on the enzyme, the sole

Received: June 27, 2012

Revised: October 30, 2012

Published: November 5, 2012



Chart 1. Chemical Structures of Lipid and Fumnonisin B1^a

^a(a) dpPC; (b) dpPA; (c) DOTAP; (d) FB1.

interaction of this mycotoxin with the surrounding membrane lipids may introduce perturbations in the environment that may affect its enzymatic activity. In this sense, perturbations of molecular organization has already been reported to modulate the *in vitro* activity of several membrane-bound enzymes like phospholipases,⁸ neuraminidase,⁹ and sphingomyelinase,¹⁰ which as well as CS, exert their catalytic activity on self-organized substrates.

The initial studies about the interaction of FB1 with model membranes were performed by Yin and co-workers. These authors found that the toxin (a) increased the oxygen transport properties of both saturated and unsaturated phosphatidylcholine (PC) bilayers,¹¹ (b) made the egg yolk phosphatidylcholine (EPC) membranes highly susceptible to oxidation,¹² and (c) perturbs the surface region of phosphatidylcholine based (PC) bilayers¹¹ and multilamellar vesicles composed of dimyristoylphosphatidylcholine (dmPC) or EPC, having minimal effects near the center of the membranes.¹³

Examination of the equilibrium conformations of FB1 in solution resulting from molecular dynamics methodology suggested that the structure is relatively extended and may not be consistent with a compact folded (globular) structure derived from previous computational studies in vacuum.¹⁴

Lately, we studied the characteristics of the initial membrane state that controls the FB1–membrane interaction and the changes in the membrane organization triggered by the toxin binding and penetration.¹⁵ It was demonstrated that FB1–lipid interactions were transduced into long-range effects at the

mesoscopic level affecting the lipidic self-separated lateral domain shape and density.

Interestingly, the results of our previous studies suggested that FB1 acquired different orientations and/or foldings depending on the surface electrostatics.¹⁵ Thus, the present paper was aimed at giving further insights into this hypothesis. With this purpose, we selected zwitterionic and charged Langmuir films as model membranes. These films were characterized in terms of their initial compressibility, polarity, and the compositional limits allowed for FB1. Then, through surface potential measurements, the collective dipolar reorientation was evaluated as a function of the molecular packing, and FB1 content and epifluorescence microscopy help correlating surface electrostatics with surface topography. Finally, with the aid of polarization-modulation infrared reflection absorption spectroscopy (PM-IRRAS) the orientation of FB1 with respect to the lipid monolayer was defined.

2. MATERIALS AND METHODS

2.1. Materials. FB1 (1,2,3-Propanetricarboxylic acid, 1,1N-[1-(12-amino-4,9,11-trihydroxy-2-methyl tridecyl)-2-(1-methylpentyl)-1,2-ethanediyl] ester) of analytical standard (purity >95%) was provided by Programme on Mycotoxins and Experimental Carcinogenesis (PROMEC, Republic of South Africa). Phospholipids and NBD-PE were from Avanti Polar Lipids (Alabaster, AL, USA). Dil C₁₈, 1,1'-dioctadecyl-3,3,3',3'-tetramethylindocarbocyanine perchlorate, was from Molecular

Probes Inc. (Eugene, OR, USA). Other drugs and solvents were of analytical grade. Chemical structures of drugs used are depicted in Chart 1.

2.2. FB1 Quantitation. The FB1 crystals (MW: 721.84) were dissolved in ethanol. FB1 was quantified in samples of this solution conveniently diluted with acetonitrile/water (1:1 v/v), as described previously.¹⁶ An aliquot (50 μL) of the diluted solution was derivatized with 200 μL of an *o*-phthaldialdehyde solution, obtained by adding 5 mL of 0.1 M sodium tetraborate and 50 μL of 2-mercaptoethanol to 1 mL of methanol containing 40 mg of *o*-phthaldialdehyde. The mycotoxin was detected and quantified with a Hewlett-Packard 1100 HPLC equipped with a fluorescence detector. The wavelengths used were 335 and 440 nm for excitation and fluorescence emission, respectively. An analytical reverse-phase C_{18} column (150 mm length by 4.6 mm internal diameter and 5 μm particle size), connected to a C_{18} precolumn (20 mm by 4.6 mm; 5 μm particle size), was used. The mobile phase was methanol/0.1 M NaH_2PO_4 at a 3:1 ratio (v/v); the pH was set at 3.35 ± 0.2 with orthophosphoric acid, and a flow rate of 1.5 mL/min was used. The quantification of FB1 was carried out by comparing the peak areas obtained for the ethanolic solution of FB1 to those corresponding to standards (purity >95%) of 10.5, 5.25, and 2.63 μg FB1 per mL (PROMEC, Republic of South Africa).

2.3. Surface Pressure–Area and Surface Potential–Area Isotherms. For the π –molecular area isotherms, π values were measured at different molecular areas of the lipids (dpPC, dpPA, DOTAP, dpPC/dpPA 3:1, or dpPC/DOTAP 3:1) containing 0 or 20 mol % of FB1 premixed in chloroform/methanol (2:1). For these experiments, we used a rectangular trough fitted with two barriers that were moved synchronously by electronic switching. Before each experiment, the trough was rinsed and wiped with 70% ethanol and several times with bidistilled water. The absence of surface-active compounds in the pure solvents and in the subphase solution (bidistilled water) was checked before each run by reducing the available surface area to less than 10% of its original value after enough time was allowed for the adsorption of possible impurities that might have been present in trace amounts. The lipid mixture dissolution (5–40 μL) was spread on the air–water interface. After 20 min, to allow solvent evaporation and monolayer stabilization, the interface was compressed with two Teflon barriers at a constant rate of 20 mm^2/s . A lower compression rate (12 mm^2/s) was tested, and identical results were obtained. Temperature was kept at 25 ± 0.5 $^\circ\text{C}$ with a water circulating bath.

The signal corresponding to the surface area (automatically determined by the KSV Minitrough from KSV Instruments, Helsinki, Finland) according to the relative position of the two compression barriers, the output from the surface pressure (π) transducer (measured automatically by the Minitrough with a platinized Pt foil 5-mm-wide \times 20-mm-long \times 0.025-mm-thick), and the surface potential (ΔV) registered by the voltage-measuring system (vibrating plate method; KSV Instruments, Helsinki, Finland) were fed into a personal computer through a serial interface using specific software. Thus, π -area and ΔV -area compression isotherms were recorded.

In addition, the values of compressibility modulus (K) as a function of molecular areas were calculated from π -area isotherms data, using eq 1:¹⁷

$$K = -(A_\pi) \cdot \left(\frac{\partial \pi}{\partial A} \right)_\pi \quad (1)$$

where A_π is the molecular area at the indicated surface pressure. This parameter reflected the physical state and allowed us to determine more precisely the bidimensional phase transition of the monolayer, when plotted against A_π . The higher the K values, the lower the interfacial elasticity was. Moreover, K values can be associated with typical two-dimensional (2D) phase states of the monolayers.

2.4. Surface Electrostatics. Surface potential (ΔV) is a measure of the electrostatic field gradient perpendicular to the membrane interface and thus varies considerably with the molecular surface density and reorientation of dipoles and changes accompanying the monolayer compression. The molecular dipole moment can be calculated according to the following equations:¹⁸

$$\Delta V = \frac{\mu_\perp}{A \cdot \epsilon_0 \cdot \epsilon_r} + \psi_0$$

$$\psi_0 = \frac{2 \cdot k_B \cdot T}{e} \cdot \sinh^{-1} \left(\frac{\sigma \cdot e}{2 \cdot \epsilon_0 \epsilon_r \cdot k_B \cdot T \cdot \kappa_D} \right)$$

$$\sinh^{-1} x = \ln(x + \sqrt{x^2 + 1}) \quad (2)$$

where ϵ_r and ϵ_0 are the relative dielectric constant and the permittivity of free space, respectively, μ_\perp is the normal component of the apparent (resultant) dipole moment per molecule, and ψ_0 is the electrostatic potential difference at the interface caused by the ionic double layer in ionized monolayers according to the Gouy–Chapman model (for uncharged monolayer, it was considered $\psi_0 = 0$),¹⁹ e , k_B , and T are the electronic charge, Boltzmann constant, and absolute temperature (298 K), respectively, and κ_D is the Debye screening length calculated according to $\kappa^{-1} = 0.304/(I^{1/2})$ for 1:1 electrolytes, where I is the ionic strength (1.5×10^{-7} M). I was determined as the concentration of counterions of charged molecules spread at the interface which were dissolved in the total trough volume (230 mL). The potential of a monolayer-free subphase ($\Delta V_0 = 0$) was taken as reference and $\epsilon_0 \approx 8.854187817620 \times 10^{-12}$ $\text{C} \cdot \text{J}^{-1} \cdot \text{m}^{-1}$.

ϵ_r is considered a macroscopic quantity, which has generated a great deal of discussion in the literature, particularly about the value it should assume. It is known that this parameter depends on the hydration as well as on the orientation and packing of the molecules in the film.²⁰ In the present work, the assumption was made that $\epsilon_r = 1$. All variables were expressed in SI units, thus μ_\perp resulted in C·m and was transformed into the more familiar debye (D) units using the equivalence $1 \text{ D} = 3.33564 \times 10^{-30}$ C·m.

2.5. Epifluorescence Microscopy of Monolayers. Lipid monolayers were prepared with chloroform/methanol 2:1 solutions of dpPC, dpPC/dpPA 3:1, or dpPC/DOTAP 3:1 (with or without FB1 at a molar fraction $x_{\text{FB1}} = 0.2$) doped with 1 mol % DiI C_{18} , and observed with an inverted epifluorescence microscope. Briefly, a KSV Minisystems surface barostat was mounted on the stage of a Nikon Eclipse TE2000-U (Tokyo, Japan) microscope, which was supplied with 20 \times long-working distance optics. The Teflon trough used had a 35-mm-diameter quartz window at its base, which allowed the observation of the monolayer through the trough. The monolayer morphology was documented with a color video camera Nikon DS-5 M with a supported resolution up to 2560–1920 pixels which represents $1231 \times 923 \mu\text{m}^2$ (capture area).

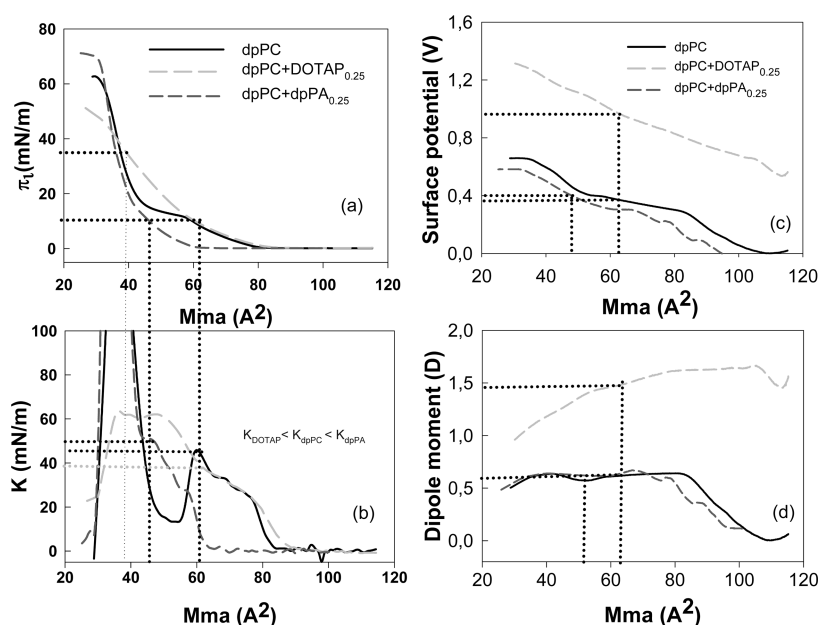


Figure 1. Elastic and electrostatic properties of the Langmuir films used. Zwitterionic (dpPC) and charged (3:1 dpPC/dpPA and 3:1 dpPC/DOTAP binary mixtures) lipids were chosen as model membranes. (a) Surface pressure (π), (b) compressibility modulus (K), (c) surface potential (ΔV), and (d) dipole moment (μ_{\perp}) are plotted as a function of the mean molecular area (Mma). Dotted lines indicate the interpolation of Mma to obtain K and μ_{\perp} at 10 and 35 mN/m (the latter is around the equilibrium surface pressures of bilayers).

After 5 min, to allow the solvent evaporation, the monolayers were compressed at a constant rate of 20 mm²/s (16 mm/min linear rate) at 25 ± 0.5 °C. Images were taken at different increasing lateral surface pressures (π). Then, the percentage of total film area contributed by regions in liquid-expanded phase (bright fluorescent areas) was calculated by analyzing the pictures with *Adobe Photoshop 7.0* software (USA).

The surface distribution of domains in the epifluorescence microscopic images of the monolayers studied was also analyzed through the radial distribution function $g(r)$ (or pair correlation function) which is considered a useful tool to describe the structure of a system. $g(r)$ gives the probability of finding a domain at the distance r from another domain and can be obtained by counting the appearance of two domains at separation r , from $r = 0$ to $r = \infty$ as shown in eq 3:²¹

$$g(r) = \frac{2}{N_p} \left\langle \sum_{i < j} \delta(r - r_{i,j}) \right\rangle \quad (3)$$

where N is the number of domains in the image, ρ is the domain surface density, r_{ij} is the position vector of domain j respect to the i th domain, and the brackets indicate average over all atoms (note that the position of a domain is defined by its mass center). Main features of $g(r)$ vs r plot are as follows: (a) a zone of excluded area ranging from $r = 0$ to ∞ , (b) a main peak corresponding to the maximal probability of finding a particle, and (c) probability at long distances tends to unity indicating absence of interdomain interactions.

2.6. Polarization-Modulation Infrared Reflection Absorption (PM-IRRAS) Spectroscopy. Polarization modulation infrared reflection-adsorption spectroscopy (PM-IRRAS) basically combines Fourier transform infrared absorption spectroscopy with modulation of the incident light beam polarization. Incident radiation was polarized in two orthogonal planes, perpendicular "s" and parallel "p", to the membrane normal.

Spectra were collected with a spectral resolution of 8 cm⁻¹, using a KSV PMI 550 PM-IRRAS (KSV Instruments Ltd., Finland), equipped with a ZnSe photoelastic modulator, operating at a frequency of 50 kHz with a variable delay on the wavelength λ . The incident light was continuously modulated between s and p polarization at a high frequency ($2f = 100$ kHz). This equipment was mounted on a KSV Minitrough. The selected angle of incidence was 80° and the maximum retardation wavelength was 1500 cm⁻¹ with a gap of 0.55 λ . These parameters allowed a high-resolution IR spectrum to be recorded within the 950–1900 cm⁻¹ wavenumber range, where most signals coming from the functional groups of phospholipid polar heads and FB1 appeared.

A differential reflectivity spectrum (eq 4) was obtained with the aid of electronic and mathematical processing of the signal. The difference (Δ) and sum (Σ) of signals (S_s and S_p) separately collected and a differential reflectivity spectrum (\hat{S}) were calculated

$$S = (S_s - S_p) / (S_s + S_p) = \Delta / \Sigma \quad (4)$$

The final PM-IRRAS spectra could then be obtained by collecting background spectra of the bare substrate ($S_{(0)}$) and the PM-IRRAS signal of the surface covered with the film ($S_{(d)}$), and calculated according to eq 5:

$$\frac{\Delta S}{S_0} = \frac{S_{(d)} - S_{(0)}}{S_{(0)}} \quad (5)$$

Monolayers were compressed up to lateral surface pressures (π) of 5, 15, 25, 35, and 45 mN/m before collecting each spectrum. Reproducibility of the π values was ±0.001 mN/m. Before the PM-IRRAS measurements, the monolayers were maintained for 5 min at the desired pressure to allow their stabilization. The baseline was acquired using a film-free air/water interface. Each spectrum was obtained with 6000 scans accumulated at a temperature of 23–25 °C.

2.7. Fourier Transformed Infrared (FT-IR) Spectra of Monolayer Components. Bulk FTIR spectra of dpPC, dpPA, DOTAP, and FB1 were recorded on a Bruker IFS 28 FTIR instrument. Solid-phase infrared spectra in the range 4000–400 cm^{-1} were recorded at room temperature with a resolution of 2 cm^{-1} from 48 co-added interferograms. When the spectra were recorded using the KBr pellet technique, a variation of the baseline was observed due to the reaction of the samples with KBr support. For that reason, all spectra were recorded on a Si(O) plate.

3. RESULTS AND DISCUSSION

3.1. Elastic and Electrostatic Surface Behavior of the Reference Langmuir Films Used. The early experiments were aimed at characterizing the films in terms of their initial compressibility and polarity. All monolayers contained dpPC (a zwitterionic lipid) in the absence or in the presence of a lipid bearing a positive (DOTAP) or negative (dpPA) charge, which was present at a 0.25 molar fraction with respect to dpPC. These mixtures were known to be stable at the air–water interface.²² The π –Mma compression isotherms are shown in Figure 1a. The film containing dpPC (solid line) showed a collapse at 54 mN/m and the typical bidimensional phase transition (BPT). Neither the film containing dpPC-DOTAP_{0.25} (dashed gray line) nor that of dpPC-dpPA_{0.25} (dashed black line) exhibited a BPT, and the former was significantly more expanded than the other ones.

To gain further insight into the surface properties of the monolayers, we analyzed the compression isotherms in terms of the compressibility modulus K , as a function of Mma. Figure 1b shows the K vs A plots, corresponding to the π – A isotherms presented in Figure 1a. The K values give information about the compactness and packing of the film. High compressibility modulus (low compressibility) is a sign that the molecules are packed tightly and the cohesive forces between them are considerable. The surface compressibility modulus can also be employed to categorize the state of Langmuir monolayers. While the K value in gaseous monolayers is known to be of the same magnitude as the surface pressure, it ranges from 12.5 to 50 mN/m for liquid expanded (LE) films, and the liquid condensed (LC) state is characterized by higher K values (within the limits of 100–250 mN/m) according to the classification of Davies and Rideal.²³

From the maximum and minimum in K –Mma isotherm (Figure 1b, solid line), the BPT of dpPC can be further characterized as starting at Mma = 60 \AA^2 and ending at Mma = 54 \AA^2 , respectively. Such a peak was not observed in the K –Mma isotherms of the mixed films. It is also noticeable that the maximal K value reached by the film containing DOTAP at the collapse point was 62 mN/m, while that of the other two films reached values much higher ($K_{\text{dpPC}} = 190$ mN/m and $K_{\text{PC-PA}} = 270$ mN/m). This indicated that the former had a LE organization along the whole compression, while the two other ones could reach the LC state at high molecular packings. However, it is interesting to recall that a monolayer resembles the behavior of a bilayer at an equilibrium surface pressure which is assumed to be around $\pi_e \cong 35$ mN/m. So, in each π –Mma isotherm at Figure 1a, we identified two π values to be carefully characterized, one of them at 35 mN/m (π_{35}) and the other one at 10 mN/m (π_{10}), which are near and below, respectively, the π_e value for bilayers. Both π were interpolated in the π –Mma compression isotherms to obtain the corresponding values of Mma which then were interpolated

in the K –Mma plot and the following K_{10} values (compressional modulus at $\pi = 10$ mN/m) were obtained: $K_{10,\text{PC-DOTAP}} = 38$, $K_{10,\text{PC}} = 44$, and $K_{10,\text{PC-PA}} = 50$ at 10 mN/m for dpPC/DOTAP_{0.25}, dpPC, and dpPC/dpPA_{0.25} films, respectively. Following similar procedures, K_{35} values (compressional modulus at $\pi = 35$ mN/m) were determined as $K_{35,\text{PC-DOTAP}} = 62$, $K_{35,\text{PC}} = 172$, and $K_{35,\text{PC-PA}} = 152$ mN/m. This allowed us to conclude that all the films analyzed were in a LE state, but pure dpPC and dpPC-dpPA_{0.25} were in a LC phase at 35 mN/m.

The electrostatic properties of the films was evaluated through ΔV –Mma compression isotherms (Figure 1c) which showed that at all compressions the DOTAP containing film was much more positive and the film containing dpPA was slightly more negative than pure dpPC with ΔV values at π_{10} of $\Delta V_{10,\text{PC-PA}} = 0.367$, $\Delta V_{10,\text{PC}} = 0.407$, and $\Delta V_{10,\text{PC-DOTAP}} = 0.950$ V. From these experimental data, the dipole moments (μ) were calculated by eq 2 (Figure 1d). A significant reorientation upon compression was observed only in the film containing DOTAP, and at π_{10} , the values for μ_{10} were as follows: $\mu_{10,\text{PC-PA}} = 630$ mD, $\mu_{10,\text{PC}} = 610$ mD, and $\mu_{10,\text{PC-DOTAP}} = 1460$ mD. At π_{35} , the surface potential values were higher than at 10 mN/m ($\Delta V_{35,\text{PC-PA}} = 0.594$, $\Delta V_{35,\text{PC}} = 0.63$, and $\Delta V_{35,\text{PC-DOTAP}} = 1.25$ V), and while $\mu_{35,\text{PC-PA}} = 630$ mD and $\mu_{35,\text{PC}} = 620$ mD remained almost constant within the experimental error, $\mu_{35,\text{PC-DOTAP}} = 1130$ mD decreased. This indicated that within the range 10–35 mN/m all the films had positively net perpendicular components of their molecular dipole moments. Differences in ΔV were observed between dpPC and dpPC/dpPA_{0.25} (more positive in the former) but disappeared in dipole moments ($\mu_{\text{PC}} \cong \mu_{\text{PA}}$), which should be ascribed to a compensation introduced by the diffused ionic layer. Only the film containing DOTAP, upon compression, suffered continuous molecular/functional group reorientations leading to a decrease in the magnitude of the resultant dipole moment from 10 to 35 mN/m, while the other films exhibited significant changes in μ_{\perp} at surface pressures closer to the collapse point. It is important to recall that μ_{\perp} is the result of contributions due to the hydrocarbon chains, the polar group, and the shell of structured water. So, the main factor introducing differences between different films is the presence of charged residues at the polar head groups.

3.2. Limits of FB1 Composition in Zwitterionic and Charged Langmuir Films As Determined from π –area Compression Isotherms and Phase Diagrams of Lipid-Toxin Pseudobinary Mixtures. π –Area Compression Isotherms. Figure 2a shows that the π –area compression isotherms of Langmuir films containing FB1 at molar fractions between $x_{\text{FB1}} = 0$ and $x_{\text{FB1}} = 1$ in mixtures with dpPC (Figure 2a), dpPC-dpPA_{0.25} (Figure 2b), and dpPC-DOTAP_{0.25} (Figure 2c).

dpPC monolayers, at $x_{\text{FB1}} \leq 0.3$, exhibited an expansion along the whole surface pressure range (from zero to collapse), mainly at $\pi < 30$ mN/m, and an increase in the bidimensional phase transition lateral pressure (π_{T}) with respect to pure dpPC. Within these FB1 proportions, the apparent collapse pressure seemed higher in the presence of the toxin compared to that of pure dpPC monolayer (e.g., at $x_{\text{FB1}} = 0.2$ $\pi_{\text{c,app,FB1-PC}} = 57$ mN/m $>$ $\pi_{\text{c,PC}} = 54$ mN/m) which might reflect the appearance of overcompressed states. At $x_{\text{FB1}} \geq 0.4$, complete isotherms were left-shifted, and the collapse points were hardly reached, suggesting a toxin-induced film destabilization within this compositional range.

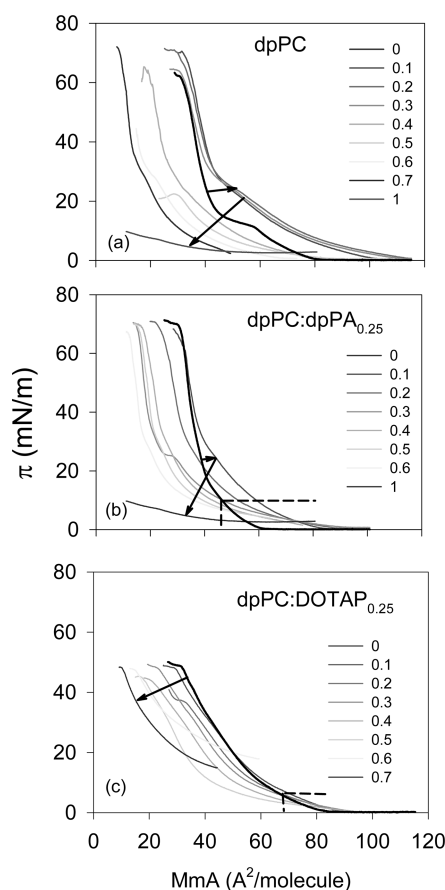


Figure 2. Effects of FB1 in the surface pressure–area (π – Mma) compression isotherms. Zwitterionic (dpPC) (panel a) and charged (3:1 dpPC/dpPA and 3:1 dpPC/DOTAP mixtures) (panels b and c) lipids with or without FB1 at molar fractions varying from 0 to 1. Upon the addition of FB1, systems are defined as binary (a) or pseudobinary (b and c) lipid–toxin mixtures. Arrows indicate the direction of isotherm displacement accompanying x_{FB1} increase. Horizontal and vertical dashed lines at the bottom of panels b and c indicate surface pressure allowing surface expansion at all compositions.

In mixtures with dpPC/dpPA_{0.25} (Figure 2b), even at $x_{FB1} = 0$, the typical bidimensional phase transition of dpPC is hardly seen, but a slope change at $\pi \cong 25$ mN/m becomes more clear upon FB1 addition to the mixture. The latter might be ascribed either to a 2D phase transition or to a partial collapse. The lack of horizontality in isotherms at this π supports the second hypothesis which is reinforced by the π – Mma phase diagram (see below). In turn, FB1 induced an expansion of the monolayer at $x_{FB1} \leq 0.2$ up to $\pi \cong 20$ mN/m and a shift to lower molecular areas (condensation or molecular lost) at higher π (Figure 2b). Higher proportion of FB1 led to left-shifted unstable isotherms, although they looked expanded at $\pi \leq 10$ mN/m at all x_{FB1} .

The whole isotherms of dpPC/DOTAP_{0.25}/FB1 ternary mixtures were left-shifted with respect to dpPC/DOTAP_{0.25} monolayers (Figure 2c) and expansions were evident below $\pi \cong 6$ mN/m at all x_{FB1} .

Contrary to what was observed in dpPC monolayers, in charged monolayers FB1 induced a decrease in the collapse pressures (e.g., at $x_{FB1} = 0.2$ $\pi_{c,dpPC:dpPA:FB1} = 57$ mN/m < $\pi_{c,dpPC:dpPA} = 63$ mN/m and $\pi_{c,dpPC:DOTAP:FB1} = 36$ mN/m < $\pi_{c,dpPC:DOTAP} = 41$ mN/m).

Mean Molecular Area–Composition Diagrams. The FB1 mixing behavior with each of the films studied was further analyzed through Mma vs x_{FB1} plots at π_{10} and π_{30} . These results are depicted in Figure 3a–c where points represent

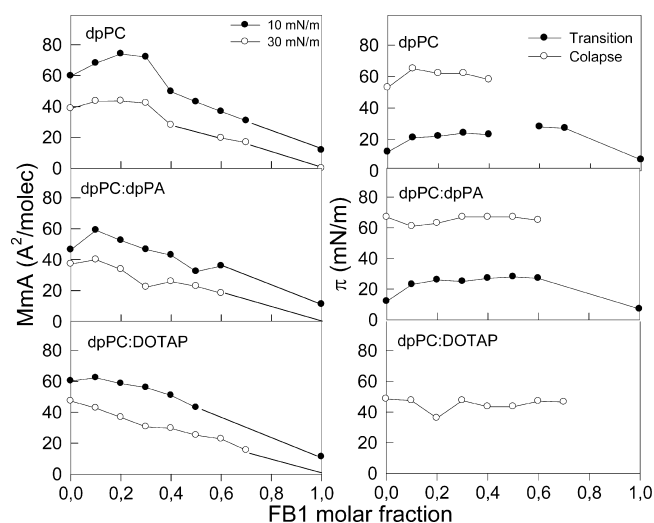


Figure 3. Stability of Langmuir films containing FB1 evaluated from Mma vs FB1 molar fraction and phase diagrams. Surface pressure– Mma (a,b,c) and phase diagrams (d,e,f) of mixtures containing dpPC (a,d), 3:1 dpPC/dpPA (b,e) or 3:1 dpPC/DOTAP (c,f) containing FB1 at different molar fractions (from $x_{FB1} = 0$ to $x_{FB1} = 1$) at two fixed surface pressures. Straight dotted lines in a, b, and c represent the ideal/immiscibility behavior. Vertical dotted lines in d, e, and f indicate approximate limits of regions I, II, and III (see text). LC and LE, liquid condensed and liquid expanded phases. * indicate states submitted to epifluorescence analysis.

experimental data (real behavior) and straight dotted lines represent the theoretical behavior of either ideal mixing or immiscibility (phase diagrams help discerning between these two possibilities). Except for dpPC/DOTAP_{0.25} films at π_{30} , which exhibited an ideal/immiscible behavior, all plots evidenced a positive deviation from ideality at low x_{FB1} . At π_{10} , upon the addition of FB1 to the zwitterionic film of dpPC Mma increased and after reaching a maximum followed a decreasing tendency and at medium proportions of FB1 reached the ideal/immiscible behavior line. In positive and negatively charged films at π_{10} , the deviation from ideality persisted along the whole x_{FB1} range. Positive deviations from ideality reflected repulsive intermolecular interactions introduced by FB1, which explained the limited amount of toxin that could be stabilized at the interface identified through the analysis of π – Mma compression isotherms. It is important to note that at π_{30} all mixtures tended to $Mma = 0$ Å²/molec at the highest x_{FB1} , which is evidence of not only an FB1-induced film destabilization, but also the high sensitivity of the film at high molecular packings.

Phase Diagrams. Phase diagram are shown in Figure 3d–f. In dpPC–FB1 mixtures, it can be identified as a region of a LE' monolayer phase containing FB1 which persisted up to $x_{FB1} \cong 0.8$ and suffered a phase transition toward a LC' phase at $\pi_T = 8$ mN/m in pure dpPC ($x_{FB1} = 0$) and increased at higher x_{FB1} reaching $\pi_T = 20$ mN/m at $x_{FB1} \cong 0.4$. The LC' is stable until the collapse at π_c that increases at very low FB1 proportions, then decreased up to $\pi = 0.4$ mN/m and could not be identified at higher x_{FB1} . Prime symbols refer to the possibility that LE'

and LC' phases could not be associated with a true phase transition but could be related to a subtle partial collapse extended along compression and leading to a continuous change in film viscosity more marked within a narrow π range. The behavior of dpPC/dpPA_{0.25} films in the presence of FB1 (Figure 3e) is similar except that the collapse could be identified up to higher x_{FB1} and the collapse point occurred at a constant π_{C} . In dpPC/DOTAP_{0.25} (Figure 3f), there was no evident phase transition and the LE phase collapsed at a π_{C} independent of x_{FB1} . The constancy in π_{C} reflects a constant film composition suggesting that it becomes saturated with FB1, the excess of which is expelled from the film.

Considering compression isotherms, Mma vs x_{FB1} , and phase diagrams together, it can be concluded that FB1 mixed mainly within the LE phase and could remain until the collapse pressure only in dpPC monolayers up to $x_{\text{FB1}} = 0.1$. Higher proportions of FB1 can be found, but up to lower π (e.g., up to $x_{\text{FB1}} = 0.4$ and π_{35}). Dotted vertical lines in Figure 3d–f mark regions of total solubility at all compressions at low x_{FB1} (I), coexistence of a three-component mixed monolayer plus a partially collapsed 3D phase at medium x_{FB1} (II), and a monolayer which upon compression recovered the properties of lipids through the expulsion of the whole amount of FB1 in equilibrium with a 3D collapsed phase at high x_{FB1} (III).

3.3. Effect of the Molar Fraction of FB1 on the Surface Electrostatics. Upon compression, the ΔV of lipid monolayers increased (Figure 4a–c) and the whole ΔV –area isotherm exhibited ΔV values following the expected order: negatively < zwitterionic < positively charged monolayers in the absence of FB1. As revealed from π –Mma isotherms, FB1 could be expelled from the monolayer depending on its molar fraction and the molecular packing. This introduced a significant uncertainty in defining real values for the surface charge density, which prevented us from obtaining reliable results for ψ_0 and thus for μ_{\perp} . So, in the case of toxin containing films, we limited the analysis to $A \times \Delta V$. This parameter represented the change in surface potential per unit of molecular density.

If compared with pure lipid monolayers, the addition of FB1 displaced the whole ΔV – A isotherms either upward, when the lipid phase was zwitterionic, or downward, in the case of mixtures containing the positively charged DOTAP. A more complex behavior was observed with the monolayer containing the negatively charged dpPA. At Mma > 48 Å²/molec, FB1 slightly displaced upward the ΔV vs Mma isotherm, and it had the opposite effect at lower Mma. The surface potential per unit of molecular area ($A \times \Delta V$) as a function of x_{FB1} (Figure 4d) was calculated at two surface compressions (10 and 30 mN/m) from data shown in Figure 4a–c. At both π studied, an increase in $A \times \Delta V$ in dpPC up to $x_{\text{FB1}} = 0.2$ and in dpPC–dpPA_{0.25} up to $x_{\text{FB1}} = 0.1$ can be observed. Deviations of $A \times \Delta V$ from ideality (imaginary line joining $A\Delta V$ values at x_{FB1} 0 and 1) followed a similar trend as deviations in Mma (Figures 3a–c) and reinforced lipids and FB1 mixing tendency and proportions.

It is important to note that $A \times \Delta V$ combined information on film stability and the complex phenomena accompanying film reorganization upon compression including changes in ϵ_r , which in turn would affect the degree of dissociation of FB1 at the interface. Discriminating the contribution of each single effect represents a challenging problem, and its solution is required to perform a proper determination of μ_{\perp} . This issue will be addressed in a future work. Meanwhile, $A \times \Delta V$ helped define composition ranges for FB1 stability at the monolayers,

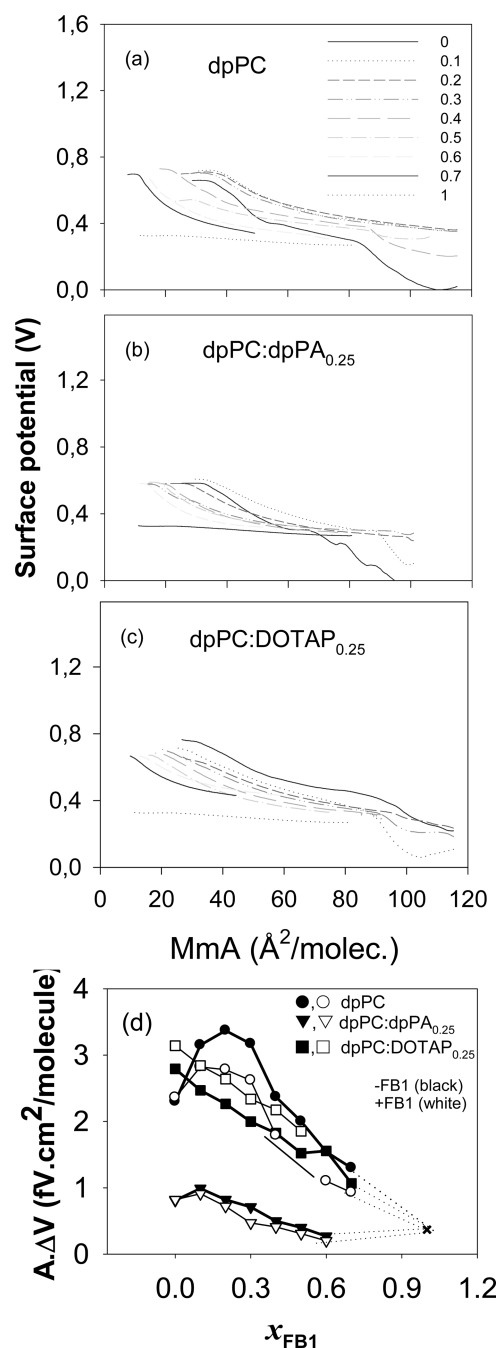


Figure 4. Stability limits of FB1 in zwitterionic and charged Langmuir films evaluated from variations in the surface charge density as a function of FB1 molar fraction. (a,b,c) ΔV vs Mma isotherms with or without FB1 (from $x_{\text{FB1}} = 0$ to $x_{\text{FB1}} = 1$). (d) Surface potential per unit of molecular area ($A \times \Delta V$) as a function of FB1 molar fraction in Langmuir films of dpPC or 3:1 dpPC/dpPA and 3:1 dpPC/DOTAP binary mixtures, at π_{10} and π_{30} . Full symbols, without FB1; Hollow symbols, with FB1.

and the information about FB1 orientation with respect to the interface was obtained from PM-IRRAS data (see below).

3.4. Effect of FB1 on the Topography of Langmuir Films. Figure 5 depicts epifluorescence micrographs of zwitterionic (a–f), negatively charged (g–i), and positively charged (m–r) lipid monolayers in the absence (a–c; g–i; m–o) and in the presence (d–f; j–l; p–r) of FB1 at $x_{\text{FB1}} = 0.2$. Data were collected at 10, 15, and 35 mN/m.

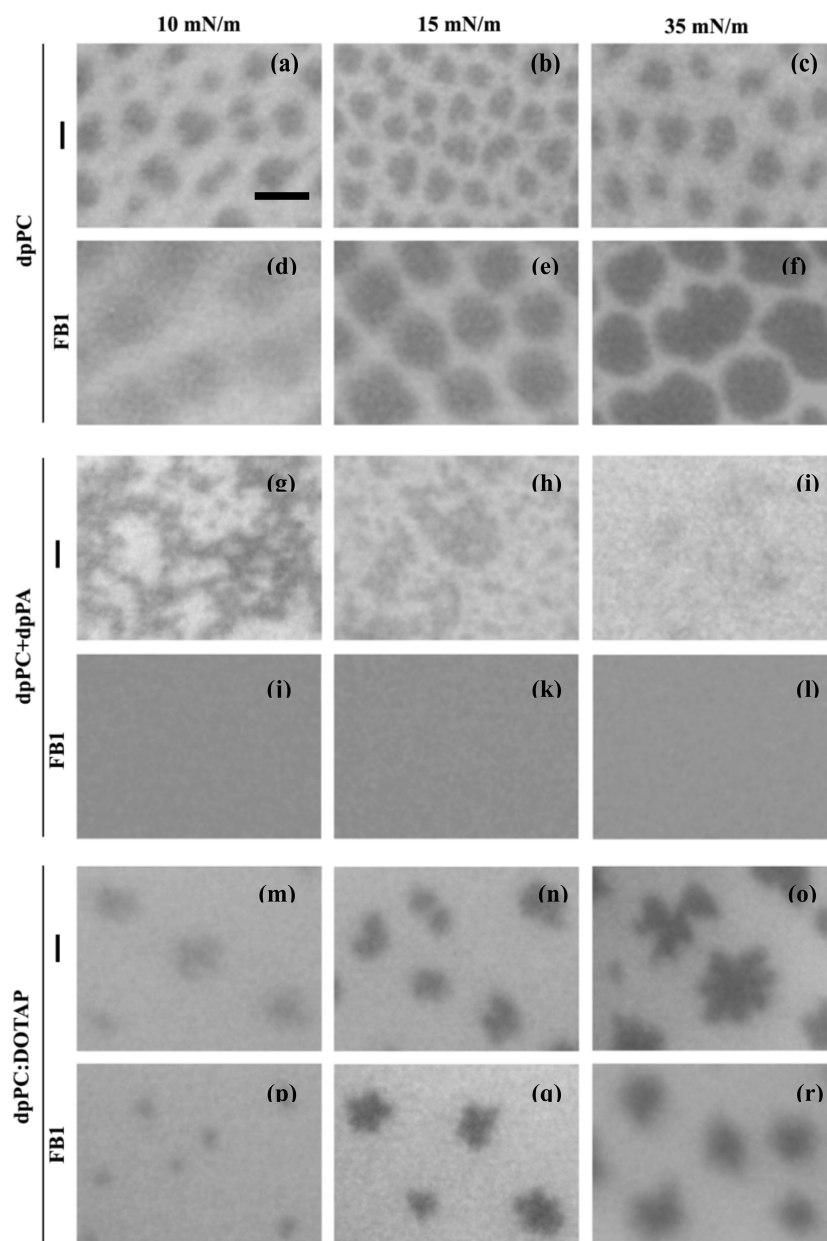


Figure 5. Effect of FB1 on the topography of zwitterionic and charged phospholipid monolayers packed at different surface pressures. Enlarged epifluorescence micrographs obtained with 20 \times ELWD lens of zwitterionic (a–f) and negatively (g–i) and positively (m–r) charged phospholipid monolayers in the absence (a–c; g–i; m–o) and the presence (d–f; j–l; p–r) of $x_{\text{FB1}} = 0.2$. Data were collected at 10, 15, and 35 mN/m. Bar represents 50 μm .

In the background of LE phase, dpPC films showed LC domains increasing in size, surface density, and complexity (lobulation degree) upon increasing the lateral surface pressure. In mixtures containing FB1, domains became bigger and rounded suggesting that FB1 increased internal repulsion within domains (LC phase). In addition, a dipole density decrease in the LE phase, due to a preferred location of FB1 in the LE phase plus possible DiIC18-FB1 electrostatic repulsions, may contribute in the same direction.

In dpPC/dpPA_{0.25} films, a fractal-shaped LC phase was observed. Fractal domains, characterized by self-similarity at different spatial scales, often appear in conditions where relaxation processes are restricted or are slower than the domain formation rate. Interestingly, in this kind of structure the formation process determines the geometry, in contrast to

what happens in organizations at the equilibrium.²⁴ In the presence of FB1 in dpPC-dpPA_{0.25} mixtures, film topography became homogeneously dark, suggesting that FB1 induced the percolation of a phase with a viscosity intermediate between LC and LE phases which is supported by the smooth slope change and the slight area expansion in π -Mma compression isotherms (Figures 2b and 3b) induced by FB1. The phenomenon would be triggered by a neutralization of the electrostatic charge supported by the increase in the surface potential density induced by FB1 in this negatively charged phospholipid mixture (Figure 4d). Furthermore, this would have thermodynamic and kinetic consequences from enhancing the mixing entropy and favoring the film relaxation rate.

dpPC-DOTAP_{0.25} monolayers also showed LC domains more lobulated and less densely distributed than those of pure

dpPC films with increasing complexity upon compression. Contrary to what was observed in dpPC-FB1 film, the presence of FB1 in dpPC-DOTAP_{0.25} induced a decrease in domain size. Multilobulation may be the result of domains that nucleate in close proximity and form a bridge that persists through the compression.²⁵ It has been discussed previously that, at least in dpPC films, multilobed domains are not stable and transform to beans over time. As well as fractality, this can also be thought of as a kinetically driven phenomenon. FB1 exerts a reduction in the surface potential density (Figure 4d) which determines a decrease in internal repulsion in domains and a decrease in the dipole density difference between phases. As a consequence, domains become smaller and rounded because relaxation processes speed up.

The radial distribution function ($g(r)$) of the domain mass centers in dpPC and dpPC/DOTAP_{0.25} in the absence and in the presence of FB1 is shown in Figure 6. Films containing

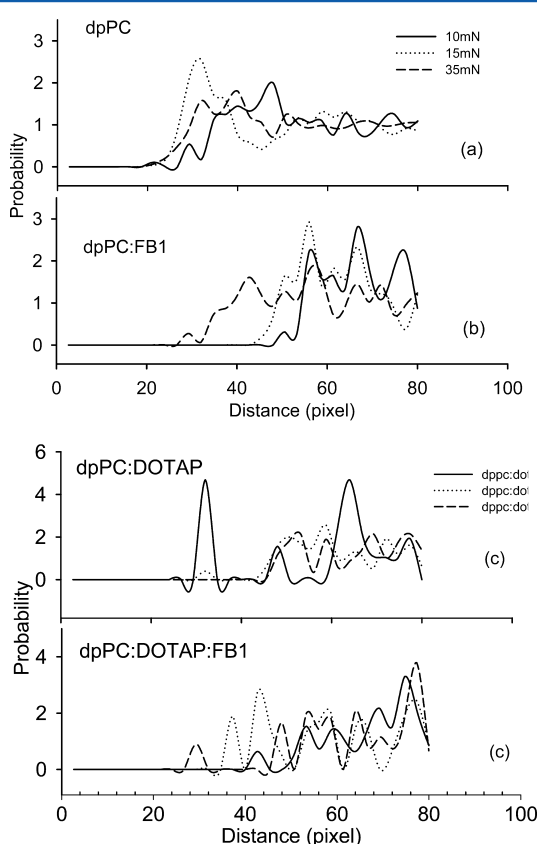


Figure 6. Effect of FB1 on the radial distribution function ($g(r)$) of 2D liquid-condensed domains in zwitterionic and charged Langmuir films. $g(r)$ was calculated according to eq 3. Patterns shown are representative of at least two replicates in each condition with similar qualitative results. One pixel represents $0.48 \mu\text{m}$.

dpPA could not be submitted to this analysis due to their fractal topography, because it was not possible to isolate structural units that can be classified as domains.

In dpPC films, the excluded distance decreased upon compression and a similar π -dependence but higher $g(r)$ values were observed in dpPC:FB1.

In dpPC/DOTAP_{0.25}, at the lowest lateral pressure $g(r)$ exhibited three peaks with a probability above the average. At $\pi \geq 15 \text{ mN/m}$, the peak corresponding to the lowest excluded distance disappeared, so domains become more separated but

more homogeneously distributed, suggesting a 2D pattern which gained simplicity at higher packings. In the presence of FB1, the excluded distance decreased upon compression with $g(r)$ values that did not tend to unity reflecting an irregular pattern of domain distribution.

3.5. Infrared Spectroscopy. PM-IRRAS at the Air–Water Interface and FT-IR Spectra in Bulk. PM-IRRAS combines the in situ characterization of the chemical composition of the surfaces of ultrathin films provided by the reflection–absorption FT-IR spectroscopy and the molecular orientation provided by the use of a photoelastic modulator (PEM). The advantage over the ordinary IRRAS mode is that modulated reflectivity is independent of isotropic adsorption from gas or bulk water, so that the interfering effects of water vapor and carbon dioxide can fairly be eliminated. We thus see that the characteristic peaks of these compounds (1640.3 and 1655.8 cm^{-1} , for bound and free water, respectively) are strongly reduced or did not appear, respectively, in the PM-IRRAS spectra, while those of the CO_2 signals (2349 and 667 cm^{-1}) are outside the energy range studied.^{26,27} Another advantage of this technique comes from the surface selection rule,²⁸ which predicts the differential infrared absorption, depending on the transition dipole vector orientation with respect to the surface normal and the angle of incidence of the IR beam. This allows us to estimate the interfacial orientation of functional groups.

It is noteworthy that, in PM-IRRAS, the absence of a peak in a spectrum does not necessarily indicate the lack of a functional group, but may be due to a random distribution (not oriented) of the absorption moments²⁶ or to some orientations of a transition dipole with respect to the normal of the membrane.²⁷ So, reference FTIR spectra of pure FB1, dpPC, dpPA, and DOTAP were recorded in the isotropic medium of a dissolution in appropriate solvent to identify all the IR signals within the wavelength range studied²⁹ and to compare them with PM-IRRAS spectra of the same compounds spread at the air–water interface and packed at lateral surface pressures between 0 and 35 mN/m .

Fumonisin B1. The FT-IR spectrum of FB1 is shown in Figure 7a. The main features are represented by signals at 1734 ,

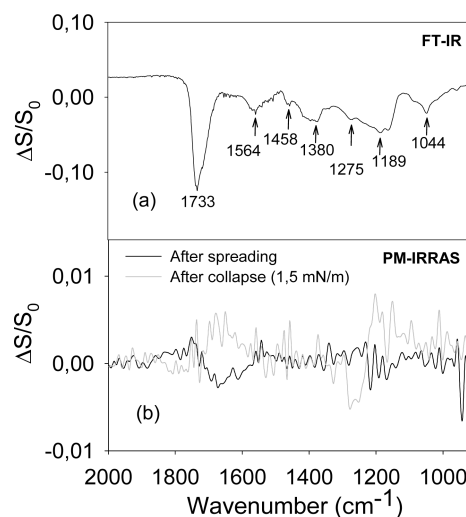


Figure 7. Infrared spectra of fumonisin B1. (a) FT-IR spectrum of FB1 in solution. (b) PM-IRRAS spectrum of FB1 at the air–water interface before and after compression.

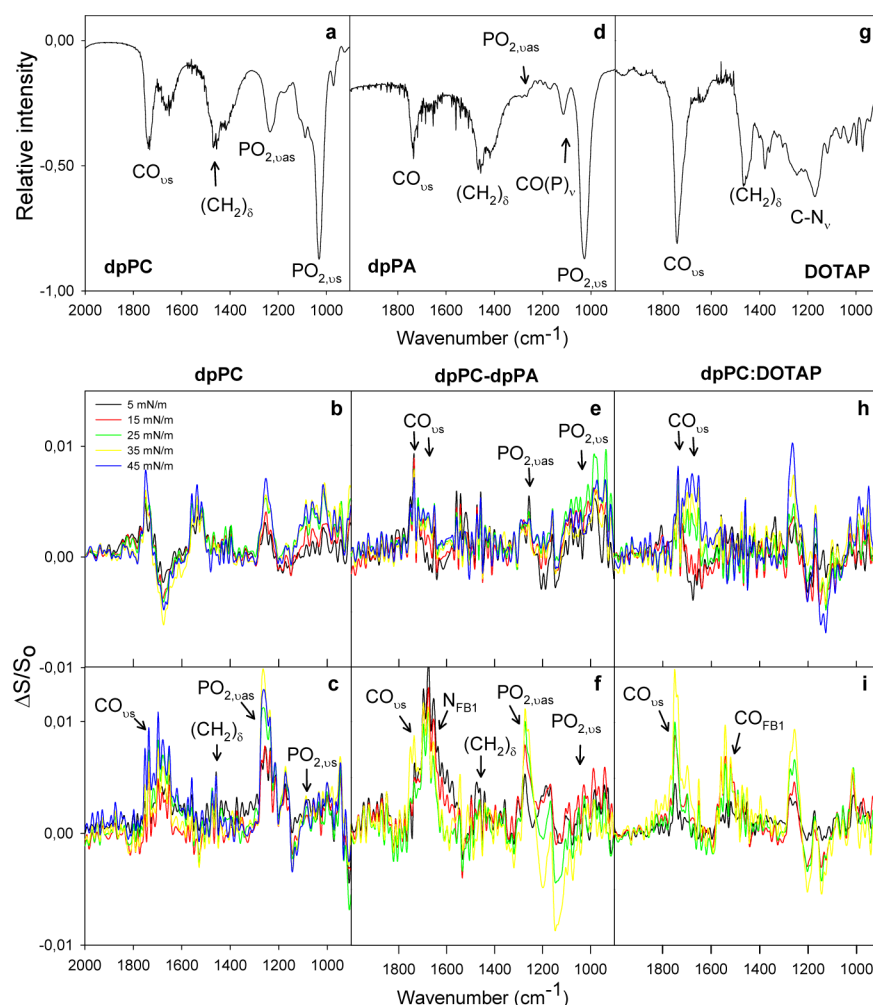


Figure 8. Effect of fumonisins B1 on the infrared spectroscopy of phospholipids in isotropic solutions and self-assembled at the air–water interface. Infrared spectroscopy of dpPC (a–c) and binary mixtures of 3:1 dpPC/dpPA (d–f) and 3:1 dpPC/DOTAP (g–i). FT-IR spectra of isotropic solutions (a,d,g) and PM-IRRAS spectra of the same lipids self-organized at the air–water interface at the indicated lateral surface pressures, in the absence (b,e,h) and in the presence (c,f,i) of FB1.

1458, and 1275 cm^{-1} belonging to carboxylate groups ($\nu(\text{C}=\text{O})$, $\delta(\text{COH})$, and $\nu(\text{C}-\text{O})$ vibrations), at 1653–1564 and 1189 cm^{-1} corresponding to the scissoring signal of primary amine group ($\delta(\text{N}-\text{H})$ and $\nu(\text{C}-\text{N})$ vibrations) and signals at 1381 and 1044 cm^{-1} were assigned to methylene and hydroxyl groups ($\delta(\text{C}-\text{H})$ and $\nu(\text{OH})$).

The general shape of the PM-IRRAS spectrum reflects the lack of coherence and marked isotropy of the film where only $\nu(\text{C}=\text{O})$ and $\delta(\text{N}-\text{H})$ signal could be identified.

The band at 1649.8 cm^{-1} is due to deformation vibration of the absorbed water molecules.³⁰

Lipids. The spectral region between 900 and 1800 cm^{-1} is very important for obtaining information on the orientation and conformational order on the subcell structure (δCH); on the hydration, H-bonding, and ion binding (e.g., νCO , νPO_2^+); as well as on the conformation of the headgroup ($\nu\text{CN}^+\text{C}$, νPO_2^-). The vibration of $\nu\text{CN}^+\text{C}$ is absent in the spectrum of dpPA.

In organic solvents, major bands in the FT-IR spectrum of dpPC corresponded to $\nu_s\text{C}=\text{O}$, $\delta(\text{CH}_2)$ (doublet), $\nu_{\text{as}}(\text{PO}_2^-)$, $\nu_s(\text{PO}_2^-)$, and $\nu_b(\text{N}(\text{CH}_3)^+)$ with frequencies located at 1739, 1470 + 1416, 1240, 1033, and 970 cm^{-1} , respectively. The band at 1660 cm^{-1} in the spectrum of Figure 8a corresponds to

residual water. Spectroscopic signals characterizing dpPA were the same (except for $\nu_b(\text{N}(\text{CH}_3)^+)$ which is absent) and were located at 1735, 1468 + 1429, 1289, and 1032 cm^{-1} corresponding to $\nu_s\text{C}=\text{O}$, $\delta(\text{CH}_2)$ (doublet), $\nu_{\text{as}}(\text{PO}_2^-)$, and $\nu_s(\text{PO}_2^-)$, respectively. DOTAP peaks were assigned as follows: 1745, 1468 + 1378, and 1254 + 1175 for $\nu_s\text{C}=\text{O}$, $\delta(\text{CH}_2)$ (doublet), and $\nu(\text{C}-\text{N})$ doublet.

At the air–water interface, dpPC can be distinguished from dpPA and DOTAP by the spectroscopic parameters of carbonyl $\nu_s(\text{C}=\text{O})$ vibrational bands, while dpPC and dpPA also differ in their phosphate vibrational signals $\nu_{\text{as}}(\text{PO}_2^-)$ and $\nu_s(\text{PO}_2^-)$. The $\nu_s(\text{C}=\text{O})$ band has a pronounced asymmetry on the low-frequency side. It consists of two overlapping components. The high-frequency component of this band is assigned to the non-hydrogen-bonded (free) carbonyl group and the lower frequency component to the hydrogen-bonded carbonyl group. Therefore, a widening of the overall CO band was observed in dpPA as well as in DOTAP spectra compared to dpPC. This can be explained with an increase in the interfacial hydration, strengthening of the hydrogen network, and reorientation of the CO transition dipole in phospholipids upon compression. An even more pronounced difference between the spectra of dpPA and that of dpPC is observed in

the phosphate vibration signals with a decrease in the integral intensity of the band in the region of $\nu_s(\text{PO}_2^-)$ and a high-frequency shifted $\nu_{as}(\text{PO}_2^-)$. Also, the absence of the $\nu_b(\text{N}(\text{CH}_3^+))$ signal at 970 cm^{-1} was found for dpPA.

Furthermore, compared with the dehydrated sample in FT-IR (Figure 8a), the PM-IRRAS spectrum of dpPC at the air–water interface exhibited two main differences: (a) the $\nu_{as}(\text{PO}_2^-)$ band located at a higher frequency (1253 cm^{-1}) and (b) the presence of a dip located at 1660 cm^{-1} (Figure 8b). It has been shown that such a shape of the PM-IRRAS band can be observed when the transition moment of the vibration associated with the band is oriented at the PM-IRRAS “magic angle” with respect to the normal of the water surface (approximately 40°).²⁷ Alternatively, the dip located at 1660 cm^{-1} has been defined as an optical effect peculiar to IRRAS, due to the strong dispersion of the refractive index of water in this spectral range (this dispersion is caused by the bending mode $\delta\text{H}_2\text{O}$).^{27,31,32} Previous numeric simulations have shown that, in first approximation, this dip is proportional to the layer thickness at the water surface³¹ and the refractive index of the media at the interface.

In the presence of FB1, the PM-IRRAS spectrum of the zwitterionic film composed of dpPC shows a pronounced asymmetry on the low-frequency side of CO signal. This signal is shifted to higher frequencies upon compression possibly reflecting the mycotoxin expulsion from the monolayer evidenced in π -Mma isotherms. Also, an increase in the $\nu_s(\text{PO}_2^-)$ signal intensity compared with the FB1 free sample is observed in dpPC monolayers.

In the negatively charged film containing dpPA, the most significant effect of FB1 is the appearance of a strong signal at 1668 cm^{-1} corresponding to $\delta(\text{N}-\text{H})$ of the primary amine group of FB1. The positively charged film containing DOTAP exhibited only the low-frequency, hydrogen-bonded component of the carbonyl $\nu_s(\text{C}=\text{O})$ and a strong signal at 1530 cm^{-1} corresponding to FB1 tricarballic acid end.

These results clearly show that the presence of FB1 has different effects on the PM-IRRAS spectrum depending on the electrostatic characteristics of the monolayer. In negatively and positively charged films, the FB1 amine and carboxylate transition dipoles, respectively, are near the interface and perpendicularly oriented with respect to the normal to the membrane. There is no evidence of the presence of these functional groups of FB1 at the interface in the zwitterionic film. This fact, in addition to the magnitude and sign in the surface potential density changes induced by FB1, supports the hypothesis of different conformation and orientations acquired by the film-bound FB1 depending on the interfacial electrostatics.

4. CONCLUSIONS

Langmuir films are valid membrane models which allow us to explore phenomena that cannot be assessed by other membrane models or by natural membranes.

In a previous paper, starting from a film-free FB1 we demonstrated the ability of this toxin to bind to membranes and to localize at the polar headgroup region modifying the interface to an extent depending on the monolayer composition, the initial molecular packing, and the subphase pH. In the present paper, we started from lipid–toxin premixtures. In combination, both studies let us discuss the reversibility of the phenomena analyzed. Both approaches

should have evolved toward the same final equilibrium state provided the system was not trapped beyond kinetic barriers.

Here, we answered three main questions: How much FB1 can be accumulated in each mixture and remain stable at the air–water interface, in different conditions of molecular packing? Is FB1 able to induce a remodeling of membrane topography? Does FB1 exhibit a significant differential preference for particular lipid–water interfaces?

Mean molecular area and surface potential vs composition data confirmed that the compositional limit of FB1 in all films was 0.25 molar fraction. Phase diagrams described a complete landscape of the molecular packing–composition phase plane. Compressibility analysis allowed us to conclude that all the toxin free films analyzed were in an LE state, but pure dpPC and dpPC-dpPA_{0.25} were in an LC phase at 35 mN/m. However, all of them exhibited a rich microstructure of LC domains. From the analysis of film topography through epifluorescence microscopy, it could be stated that FB1 seemed to decrease the film relaxation rate, decrease internal repulsion within domains, and decrease the dipole density difference between phases. This may be considered the mirror image of the lateral expansion occurring upon FB1 penetration in toxin free film described previously. Changes in membrane topography have a significant biological relevance, because this could be related to the remodeling of membrane raft-like structures, which are considered to be platforms for functional proteins. Among these proteins might be enzymes associated with the sphingolipid metabolism which are proposed as mediators of FB1 toxic effect. In that case, the molecular mechanism of FB1 is not required to be exerted on the enzyme but can have an indirect effect on the environmental organization (raft-like structures remodeling) leading to changes in the enzyme conformation and function.

Also, comparing previous and present results, it can be concluded that electrostatic changes induced by the presence of FB1 in lipidic monolayers were of the same sign independent of the direction from which the toxin came to the system (binding from the milieu or premixed with lipids) suggesting that equilibrium in FB1 orientation could be achieved. Furthermore, the remarkable evidence suggesting that FB1 adopted different orientations and/or foldings depending on the combined charge states of the toxin and the binding surface here could be confirmed by PM-IRRAS analysis. Results clearly showed that amine and carboxylate transition dipoles were located close to the interface, were oriented in the direction perpendicular with respect to the normal to the membrane, and required the acquisition of extended conformation. This would favor the electrostatic alignment of FB1 with lipid charge residues leading to charge neutralization expressed by a compensation of the surface potential. Furthermore, in zwitterionic films the globular conformation should be acquired so that FB1 can bind to the interface through a short hydrophobic chain leaving the charged functional groups far from the interface. Thus, the globular-extended conformational equilibrium of FB1 is dynamically defined by the sign of the membrane surface charge.

Present results suggest that the molecular flexibility of FB1 is responsible for its conformational equilibrium. This turns into a functional flexibility contributing to amplifying the spectrum of FB1 membrane binding sites and becoming a toxicity enhancing factor that is absent in rigid molecules.

Taken together, the present results reinforced the lipid organization-mediated hypothesis of FB1 toxicity.

AUTHOR INFORMATION

Corresponding Author

*Phone: (+54)(+351) 434 4983 (Ext. 5). Fax: (+54)(+351) 433 4139. E-mail: mperillo@efn.uncor.edu.

Notes

The authors declare no competing financial interest.

ACKNOWLEDGMENTS

Authors acknowledge Dr. W. J. Peléaz from INFIQ (CONICET-Depto. Físico-Química, Fac. Cs. Químicas, UNC) Argentina for his help with the recording of FT-IR spectra in bulk. This work was partially supported by grants from SeCyT-UNC, Agencia Nacional de Ciencia y Tecnología grants PICT2007-00685, PICT2010 no 1232, Ministerio de Ciencia y Tecnología de Córdoba grant no 0279-005429/2006, and CONICET. P.D.C. holds a doctoral fellowship and M.G.T. and M.A.P. are career investigators of the latter institution.

ABBREVIATIONS

BPT, bidimensional phase transition; Dil C₁₈, 1,1'-dioctadecyl-3,3,3',3'-tetramethylindocarbocyanine perchlorate; dpPA, 1,2-Dipalmitoyl-*sn*-Glycero-3-Phosphate; dpPC, 1,2-Dipalmitoyl-*sn*-Glycero-3-Phosphocholine; DOTAP, 1,2-Dioleoyl-3-Trimethylammonium-Propane; FB1, fumonisin B1; NBD-PE, 1,2-Dipalmitoyl-*sn*-Glycero-3-Phosphoethanolamine-N-(7-nitro-2-1, 3-benzoxadiazol-4-yl); ν , δ , r , and w , stretching, bending, rocking, and wagging vibrational modes, respectively

REFERENCES

- (1) Meggs, W. J. *Toxicology and Industrial Health* **2009**, *25* (9–10), 571–6.
- (2) Brase, S.; Encinas, A.; Keck, J.; Nising, C. F. *Chem. Rev.* **2009**, *109* (9), 3903–90.
- (3) Rheeder, J. P.; Marasas, W. F.; Vismar, H. F. *Appl. Environ. Microbiol.* **2002**, *68* (5), 2101–5.
- (4) Bolger, M.; Coker, R. D.; DiNovi, M.; Gaylor, D.; Gelderblom, W.; Olsen, M.; Paster, N.; Riley, R. T.; Shephard, G.; Speijers, G. J. A. *JECFA, FAO Food and Nutrition Paper 74/Food Additives Series 47*; World Health Organization, 2001.
- (5) Merrill, A. H., Jr; van Echten, G.; Wang, E.; Sandhoff, K. *J. Biol. Chem.* **1993**, *268* (36), 27299–306. Merrill, A. H., Jr; Vales, T. R.; Smith, E. R.; Schroeder, J. J.; Menaldino, D. S.; Alexander, C.; Crane, H. M.; Xia, J.; Liotta, D. C.; Meredith, F. I.; Riley, R. T. *Adv. Exp. Med. Biol.* **1996**, *392*, 297–306.
- (6) Bionda, C.; Portoukalian, J.; Schmitt, D.; Rodriguez-Lafrasse, C.; Ardail, D. *Biochem. J.* **2004**, *382* (Pt2), S27–33.
- (7) Venkataraman, K.; Riebeling, C.; Bodennec, J.; Riezman, H.; Allegood, J. C.; Sullards, M. C.; Merrill, A. H., Jr; Futerman, A. H. *J. Biol. Chem.* **2002**, *277* (38), 35642–9.
- (8) Lichtenberg, D.; Romero, G.; Menashe, M.; Biltonen, R. L. *J. Biol. Chem.* **1986**, *261* (12), 5334–40. Perillo, M. A.; Guidotti, A.; Costa, E.; Yu, R. K.; Maggio, B. *Mol. Membr. Biol.* **1994**, *11* (2), 119–26.
- (9) Perillo, M. A.; Yu, R. K.; Maggio, B. *Biochim. Biophys. Acta* **1994**, *1193* (1), 155–64.
- (10) De Tullio, L.; Maggio, B.; Hartel, S.; Jara, J.; Fanani, M. L. *Cell Biochem. Biophys.* **2007**, *47* (2), 169–77.
- (11) Yin, J. J.; Smith, M. J.; Eppley, R. M.; Page, S. W.; Sphon, J. A. *Biochem. Biophys. Res. Commun.* **1996**, *225* (1), 250–5.
- (12) Yin, J. J.; Smith, M. J.; Eppley, R. M.; Page, S. W.; Sphon, J. A. *Biochim. Biophys. Acta* **1998**, *1371* (1), 134–42.
- (13) Yin, J. J.; Smith, M. J.; Eppley, R. M.; Troy, A. L.; Page, S. W.; Sphon, J. A. *Arch. Biochem. Biophys.* **1996**, *335* (1), 13–22.
- (14) Momany, F. A.; Dombrink-Kurtzman, M. A. *J. Agric. Food Chem.* **2001**, *49* (2), 1056–61.
- (15) Theumer, M. G.; Clop, E. M.; Rubinstein, H. R.; Perillo, M. A. *Colloids Surf., B* **2008**, *64* (1), 22–33.
- (16) Shephard, G. S.; Sydenham, E. W.; Thiel, P. G.; Gelderblom, W. C. A. *J. Liq. Chromatogr.* **1990**, *13*, 2077–2087.
- (17) Marsh, D. *Biochim. Biophys. Acta* **1996**, *1286* (3), 183–223. Sanchez, J. M.; Perillo, M. A. *Biophys. Chem.* **2002**, *99* (3), 281–95.
- (18) Gaines, G. L. *Insoluble monolayers at liquid-gas interfaces*, 1st ed.; Intersciences Publishers: New York, 1966; p 386.
- (19) Perillo, M. A.; Polo, A.; Guidotti, A.; Costa, E.; Maggio, B. *Chem. Phys. Lipids* **1993**, *65* (3), 225–38.
- (20) Warszynski, P.; Barzyk, W.; Lunkenheimer, K.; Fruhner, H. J. *Phys. Chem. B* **1998**, *102*, 10948–10957. Dynarowicz-Latka, P.; Dhanabalan, A.; Oliveira, O. J. *Adv. Colloid Interface Sci.* **2001**, *91* (2), 221–293.
- (21) Chavez-Castillo, M. R.; Rodriguez-Meza, M. A.; Meza-Montes, L. *2D Radial Distribution Function of Silicene*; arXiv:1112.5204v1 [cond-mat.mtrl-sci] [Online], 2011, (Accessed 05 Feb 2012).
- (22) Varas, M.; Sanchez-Borzone, M.; Sanchez, J. M.; Barioglio, S. R.; Perillo, M. A. *J. Phys. Chem. B* **2008**, *112* (24), 7330–7.
- (23) Davies, J. T.; Rideal, E. K. *Interfacial phenomena*, 2nd ed.; Academic Press Inc.: New York, 1963; p 480.
- (24) Poon, W. C. K.; Haw, M. D. *Adv. Colloid Interface Sci.* **1997**, *73*, 71–126.
- (25) McConlogue, C. W.; T.K., V. *Langmuir* **1997**, *13*, 7158–7164.
- (26) Blaudez, D.; Buffeteau, T.; Cornut, J. C.; Desbat, B.; Escafre, N.; Pezolet, M.; Turlet, J. M. *Appl. Spectrosc.* **1993**, *47* (7), 869–874.
- (27) Blaudez, D.; Turlet, J.-M.; Dufourcq, J.; Bard, D.; Buffeteau, T.; Desbat, B. *J. Chem. Soc., Faraday Trans.* **1996**, *92* (4), 525–530.
- (28) Buffeteau, T.; Desbat, B. *Appl. Spectrosc.* **1989**, *43* (6), 1027–1032.
- (29) Silverstein, R. M.; Webster, F. X.; Kiemble, D. J. *Spectrometric identification of organic compounds*, 7th ed.; John Wiley & Sons, Inc.: Danvers, 2005.
- (30) Wong, S.-S.; Kasapis, S.; Tan, Y. M. *Carbohydr. Polym.* **2009**, *77* (2), 280–287.
- (31) Buffeteau, T.; Blaudez, D.; Péré, E.; Desbat, B. *J. Phys. Chem. B* **1999**, *103* (24), 5020–5027.
- (32) Dluhy, R. A. *J. Phys. Chem.* **1986**, *90* (7), 1373–1379.